Monthly Notices
of the
ROYAL ASTRONOMICAL SOCIETY

MNRAS **488,** 5690–5701 (2019)
Advance Access publication 2019 July 30

doi:10.1093/mnras/stz2089

Full-3D relativistic MHD simulations of bow shock pulsar wind nebulae: emission and polarization

B. Olmi [1,2,3]★ and N. Bucciantini [1,4,5]

[1] *INAF – Osservatorio Astrofisico di Arcetri, Largo E. Fermi 5, I-50125 Firenze, Italy*
[2] *Institute of Space Sciences (ICE, CSIC), Campus UAB, Carrer de Magrans s/n, E-08193 Barcelona, Spain*
[3] *Institut d'Estudis Espacials de Catalunya (IEEC), E-08034 Barcelona, Spain*
[4] *Dipartimento di Fisica e Astronomia, Università degli Studi di Firenze, Via G. Sansone 1, I-50019 Sesto F. no (Firenze), Italy*
[5] *INFN – Sezione di Firenze, Via G. Sansone 1, I-50019 Sesto F. no (Firenze), Italy*

Accepted 2019 July 26. Received 2019 July 26; in original form 2019 June 27

ABSTRACT

Bow shock pulsar wind nebulae are observed with a variety of complex morphologies at different wavelengths, most likely due to differences in the magnetic field strength and pulsar wind geometry. Here we present a detailed analysis, showing how these differences affect the observational properties in these systems, focusing on non-thermal synchrotron emission. By adopting different prescriptions for the local emissivity, on top of the magnetic and flow patterns taken from three-dimensional (3D) high-resolution numerical simulations in relativistic magnetohydrodynamics (MHD), and considering various viewing angles, we try to characterize the main features of the emission and polarization, to verify if and how these can be used to get information, or to put constraints, on known objects. We found, for example, that conditions leading to a strong development of the turbulence in the bow shock tail produce substantial differences in the emission pattern, especially in polarized light.

Key words: polarization – radiation mechanisms: non-thermal – relativistic processes – methods: numerical – pulsars: general – ISM: supernova remnants.

1 INTRODUCTION

Bow shock pulsar wind nebulae (BSPWNe) are a peculiar subclass of the larger set of pulsar wind nebulae (PWNe), defined broadly as non-thermal synchrotron emitting sources powered by the spin-down luminosity of a pulsar (Gaensler & Slane 2006). Unlike systems where the pulsar is still confined in the parent supernova remnant (SNR), and where the PWN is observed with a centre-filled morphology, BSPWNe involve older objects, where the pulsar is directly interacting with the interstellar medium (ISM; in a few cases BSPWNe are seen also for pulsars interacting with the SNR shell). It is in fact estimated that a consistent fraction, between 10 and 50 per cent, of all the pulsars is born with a kick velocity in the range 100–500 km s^{-1} (Cordes & Chernoff 1998; Arzoumanian, Chernoff & Cordes 2002; Sartore et al. 2010; Verbunt, Igoshev & Cator 2017), while the progenitor remnant is in decelerated expansion (Cioffi, McKee & Bertschinger 1988; Truelove & McKee 1999; Leahy, Green & Tian 2014; Sánchez-Cruces et al. 2018). They are thus fated to leave their parent SNR on short time-scales if compared with the typical pulsar ages ($\sim 10^3$ yr versus $\sim 10^6$ yr).

Given that the typical sound speed in the ISM is of order 10–100 km s^{-1}, well below the typical pulsar velocities, as soon as the star leaves the SNR shell and starts to interact directly with the ISM, its motion becomes strongly supersonic. The balance of the pulsar wind ram pressure with the ram pressure of the surrounding ISM through which it moves induces the formation of a bow shock (Wilkin 1996; Bucciantini & Bandiera 2001; Bucciantini 2002), characterized by an elongated cometary morphology, with the pulsar located at the head of a long tail of plasma, extending in the direction opposite to its motion. As in the case of other PWNe, the relativistic pulsar wind shocked and decelerated into a strong termination shock, inflates within this cometary nebula a bubble of relativistic particles and magnetic fields, which is a synchrotron emitter, form radio to X-rays. Indeed many of such systems have been identified in recent years as non-thermal sources (Arzoumanian et al. 2004; Gaensler et al. 2004; Chatterjee et al. 2005; Gaensler 2005; Li, Lu & Li 2005; Yusef-Zadeh & Gaensler 2005; Kargaltsev et al. 2008, 2017; Misanovic, Pavlov & Garmire 2008; Hales et al. 2009; Ng et al. 2009, 2010, 2012; De Luca et al. 2011; Marelli et al. 2013; Jakobsen et al. 2014; Klingler et al. 2016b; Posselt et al. 2017). For a few of these objects radio polarimetric data are also available, pointing to a variety of magnetic configurations (Yusef-Zadeh & Gaensler 2005; Ng et al. 2010, 2012; Klingler et al. 2016a; Kargaltsev et al. 2017).

★ E-mail: barbara@arcetri.astro.it

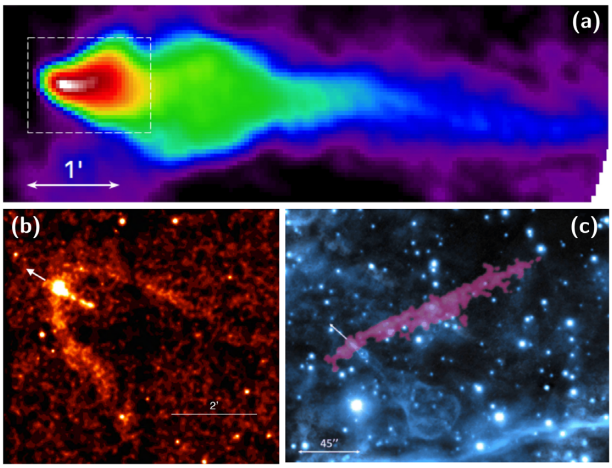

Figure 1. Selected sample of a few famous BSPWNe: (a) the Mouse nebula in radio (Very Large Array, VLA); (b) Geminga in a combined X-ray image (*Chandra*-Advanced CCD Imaging Spectrometer, ACIS, 0.5–8 keV, 540 s); (c) the Guitar nebula and its mysterious misaligned outflow in a combined Hα X-ray image (*Chandra*-ACIS, 0.5–8 keV, 195 ks) taken from the *Chandra* archives.

In the case of pulsars moving in an ISM with neutral hydrogen these nebulae can be observed in Hα emission (Kulkarni & Hester 1988; Cordes, Romani & Lundgren 1993; Bell et al. 1995; van Kerkwijk & Kulkarni 2001; Jones, Stappers & Gaensler 2002; Brownsberger & Romani 2014; Romani, Slane & Green 2017), due to charge exchange and collisional excitation processed with the shocked ISM material (Chevalier, Kirshner & Raymond 1980; Hester, Raymond & Blair 1994; Bucciantini & Bandiera 2001; Ghavamian et al. 2001), or alternatively in the ultraviolet (UV; Rangelov et al. 2016) and infrared (IR; Wang et al. 2013). It is debatable if many extended and morphologically complex TeV sources detected by the High Energy Stereoscopic System (H.E.S.S.) in coincidence with pulsars, can be attributed to the BSPWN class (Kargaltsev, Pavlov & Durant 2012), especially in those cases where the pulsar is strongly offsetted from the centre of emission. An example of this kind of uncertainty is represented by the young and energetic PSR J05376−6910 from the Large Magellanic Cloud, which is not uniquely identified as a bow shock nebula due to the large distance (Kargaltsev et al. 2017).

In Fig. 1, we present a selection of BSPWNe to highlight the variety of the typical morphologies that are observed.

(i) The Mouse nebula was first observed in a radio survey of the Galactic Centre (Yusef-Zadeh & Bally 1987) and it shows one of the most extended radio tails ever seen (Gaensler et al. 2004; Hales et al. 2009). In the head it is quasi-conical with half-aperture angle of $\sim$25° and gets narrower at a distance of $\sim$1 arcmin behind the pulsar. It is also one of the few BSPWNe for which we have polarimetric information, suggesting a magnetic field wrapped around the bow shock head and then becoming parallel to the pulsar motion in the tail (Yusef-Zadeh & Gaensler 2005). Interestingly X-rays show a more compact tail, more than a factor of 10 fainter than the head, with signs of diffuse emission in a halo ahead of the pulsar itself. Deep observations in the X-ray band have been presented recently by Klingler et al. (2018), showing a clearer picture of the PWN. The tail shows an evident narrowing with the distance from the pulsar and a smaller lateral expansion with respect to the radio structure.

(ii) The PWN associated with Geminga, on the other hand, is only observed in X-rays. It shows an asymmetric three-tail morphology with a long central tail (Posselt et al. 2017), apparently formed by isolated blobs, surrounded by two lateral tails (Caraveo et al. 2003; Pavlov, Sanwal & Zavlin 2006; Pavlov, Bhattacharyya & Zavlin 2010), which show a hard spectrum with no signs of synchrotron cooling, and are not just due to limb brightening.

(iii) A peculiar case is that of the Guitar nebula, observed in Hα (Cordes et al. 1993; Dolch et al. 2016). Different attempts to find an X-ray counterpart compatible with the revealed Hα morphology have failed, while high-resolution observations made with *Chandra* revealed, on the contrary, a misaligned X-ray outflow, inclined by $\sim$118° with respect to the direction of the pulsar motion (Wong et al. 2003; Hui & Becker 2007; Johnson & Wang 2010). The Hα shape also presents a peculiar 'head-and-shoulder' configuration, with an evident broadening with distance from the pulsar, possibly the evidence of the mass loading of neutrals from the ambient matter (Morlino, Lyutikov & Vorster 2015; Olmi, Bucciantini & Morlino 2018). Recently a similar X-ray feature has been also seen in the Lighthouse nebula (Pavan et al. 2014; Marelli et al. 2019).

Recent observations have also revealed extended TeV haloes surrounding some BSPWNe (Abeysekara et al. 2017), though to be the signature of the escape of high-energy particles. If so, one could use them to constrain the contribution of PWNe to leptonic antimatter in the Galaxy (Blasi & Amato 2011; Amato & Blasi 2018).

The firsts numerical models of BSPWNe dated from the past decade (Bucciantini 2002; van der Swaluw et al. 2003; Bucciantini, Amato & Del Zanna 2005; Vigelius et al. 2007). By using multi-dimensional codes it was possible to extend the simple analytical or semi-analytical models (Bandiera 1993; Wilkin 1996) to account for the presence of magnetic field or anisotropy in either the wind or the ISM. However, only recently results from the first three-dimensional (3D) simulations of BSPWNe in the fully relativistic magnetohydrodynamics (MHD) regime were presented by Barkov, Lyutikov & Khangulyan (2019), where the authors investigate the morphology resulting from a few different assumptions for the magnetic field geometry and properties of the ambient medium. At the same time in Olmi & Bucciantini (2019, hereafter Paper I), we presented a large set of 3D relativistic MHD simulations performed with adaptive mesh refinement (AMR) to improve the numerical resolution at the bow shock head, in an attempt to sample as much as possible the parameter space characteristic of these systems. Different models for the pulsar wind were taken into account, implementing both isotropic and anisotropic distribution of the energy flux, with diverse values of the initial magnetization, and defining a set of various geometries by varying the inclination of the pulsar spin-axis with respect to the pulsar kick velocity. In Paper I, we analysed the effects of the variation of the pulsar wind properties on the global morphology of the BSPWN, and on its dynamics, with particular attention to the development of turbulence in the tail.

This paper is the follow-up of our previous work. Here we present emission and polarization maps computed on top of our previous simulations, focusing the discussion on the possible observational signatures. In particular we will try to assess the role of turbulence in the emission properties, the possible way to distinguish laminar versus turbulent flows, and how to use this information to guess the geometry of the system. Recently a simplified emission model for purely laminar flows has been presented by Bucciantini (2018a), also used to evaluate the possible escape of high-energy particles

in Bucciantini (2018b), and we will compare our result with those predictions.

The paper is organized as follows: in Section 2, we recall the different models considered in our numerical analysis from Paper I, and briefly describe the methods used to compute emission and polarimetric maps; in Section 3, we present the complete analysis of the results, comparing them with previous models; in Section 4, we sum up our findings and draw our conclusions.

2 METHODS

The 3D structure of the velocity and magnetic field is provided by our 3D relativistic MHD (RMHD) models, developed and presented in Paper I, to which the reader is referred for a general discussion of the set-up. Given that in all of those models the ISM was assumed to be unmagnetized, the magnetic field, injected by the pulsar wind, can be taken as a good tracer of the relativistic material coming from the pulsar itself, and defining the part of the tail that is responsible for non-thermal emission. Moreover, we will concentrate here on radio emission, and radio emitting particles have synchrotron lifetime longer that the flow time in the nebula, so that we can neglect cooling. Let us note here that given the typical high flow speed found in numerical simulations, even X-ray emitting particles are only marginally affected by cooling (Bucciantini et al. 2005), such that our results can reasonably apply even to higher energies.

We assume, following Del Zanna et al. (2006), that the emitting pairs are distributed according to a power law in the energy ϵ, $n(\epsilon) = K\epsilon^{-(2\alpha+1)}$, where K is proportional to the local density of emitting particles, and their local synchrotron emissivity at frequency ν, toward the observer, is

$$j(\nu, \boldsymbol{n}) = C|\boldsymbol{B}' \times \boldsymbol{n}'|^{\alpha+1} D^{\alpha+2} \nu^{-\alpha}, \tag{1}$$

where $\boldsymbol{B}'$ and $\boldsymbol{n}'$ are, respectively, the magnetic field and the observer direction measured in the frame comoving with the flow, while C is a normalization constant dependent on K. D is the Doppler boosting coefficient,

$$D = \frac{\sqrt{1-\beta^2}}{1-\boldsymbol{\beta}\cdot\boldsymbol{n}} = \frac{1}{\gamma(1-\boldsymbol{\beta}\cdot\boldsymbol{n})}, \tag{2}$$

where γ is the Lorentz factor of the flow, $\boldsymbol{\beta}$ and $\boldsymbol{n}$, respectively, the flow speed normalized c, and the observer direction, both measured in the observer frame. Now, in terms of quantities measured in the observer frame (unprimed), one has

$$|\boldsymbol{B}' \times \boldsymbol{n}'| = \frac{1}{\gamma}\sqrt{B^2 - D^2(\boldsymbol{B}\cdot\boldsymbol{n})^2 + 2\gamma D(\boldsymbol{B}\cdot\boldsymbol{n})(\boldsymbol{B}\cdot\boldsymbol{\beta})}. \tag{3}$$

One can also compute the polarization angle ξ that enters into the definition of the Stoke's parameters Q and U (Bucciantini & Olmi 2018). Choosing a Cartesian reference frame with the observer placed in the X direction, one finds

$$\cos 2\xi = \frac{q_Y^2 - q_Z^2}{q_Y^2 + q_Z^2}, \qquad \sin 2\xi = -\frac{q_Y q_Z}{q_Y^2 + q_Z^2}, \tag{4}$$

where

$$q_Y = (1-\beta_X)B_Y + \beta_Y B_X, \qquad q_Z = (1-\beta_X)B_Z + \beta_Z B_X. \tag{5}$$

In general the local density of emitting particles K, as well as the power-law index α, might differ in different locations, depending on how particles are injected. For simplicity we assume that the power-law index α is uniform in the nebula. For the emitting particle density we adopt two different choices: either a uniform distribution, as was done in Bucciantini (2018a), or a density proportional to the local values of the thermal pressure, as it is customary in other PWNe models (Volpi et al. 2008; Olmi et al. 2014). We have also investigated a third possibility that the emission is concentrated in the current sheets that form in the BSPWN. In this case their local synchrotron emissivity at frequency ν, toward the observer, is taken to be

$$j(\nu, \boldsymbol{n}) = C_J \|\boldsymbol{J}\| D^{\alpha+2} \nu^{-\alpha}, \tag{6}$$

where $\boldsymbol{J}$ is the current density, computed as the curl of $\boldsymbol{B}$ (we have verified that the displacement current is negligible), and C_J is just a normalization constant that we assume to be position independent. In this case we also compute polarization just by taking as the polarization direction the one given by the local magnetic field. Note that ohmic dissipation should scale as $\|\boldsymbol{J}\|^2$, however, because of the use of AMR, given that the resistivity is purely numerical in nature, such choice leads to artificial jumps in the surface brightness in coincidence with AMR refinement boundaries, given that $\|\boldsymbol{J}\|^2$ it is not volume conserved. This spurious effect is strongly mitigated if one takes the simple norm of the current, given that this quantity is instead volume conserved in ideal MHD.

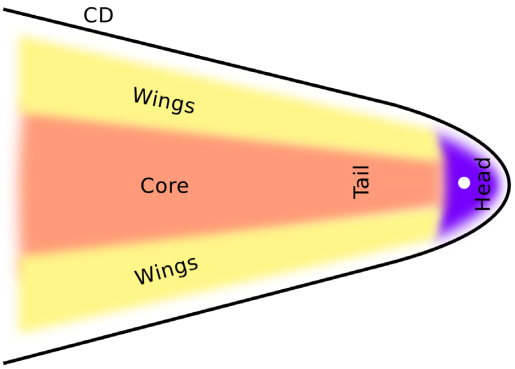

Figure 2. Scheme of the BSPWN structure: the nebula is divided into the head, the region surrounding the pulsar, and the tail. The last one is further divided in three different regions: a central core surrounded by wings that allow an easier interpretation of the emitting and polarimetric properties.

3 EMISSION MAPS

We build all of our maps using a spectral index $\alpha = 0$. Bucciantini (2018a) showed that this is a good average for the observed radio spectra, and changes in the typical observed range do not affect much the results. The polarized fraction (PF) is always given in terms of the theoretical maximum, which is 0.6 for $\alpha = 0$. To keep the discussion as simple as possible, we have schematized the BSPWN as shown in Fig. 2, highlighting the key regions whose properties we are going to discuss, and compare.

Emission maps where computed for all simulations presented in Paper I. We adopt here the same notation for the names of the different reference RMHD models, while for the emission maps we use a different notation, which allows one to identify them in terms of the physical parameters. The new notations ISO-Aj-Sx and ANI-Aj-Sx refer to the model $I_{\{\phi_M,\, i\}}$ and $A_{\{\phi_M,\, i\}}$ of Paper I, with $x = 10^{-i}$ (referring to $\sigma = [0.01,\ 0.1,\ 1.0]$) and $j = 180\phi_M/\pi$ (the spin-to-kick inclination in degrees) as shown Fig. 3, where we show also the trend toward more turbulent configurations.

In Fig. 4, we illustrate the typical viewing geometry we use to build our maps. We sampled the full range of possible inclination angles $\mathcal{X} = [0°, 360°]$. However as it was done in Bucciantini (2018a), to keep the discussion as simple as possible, focusing

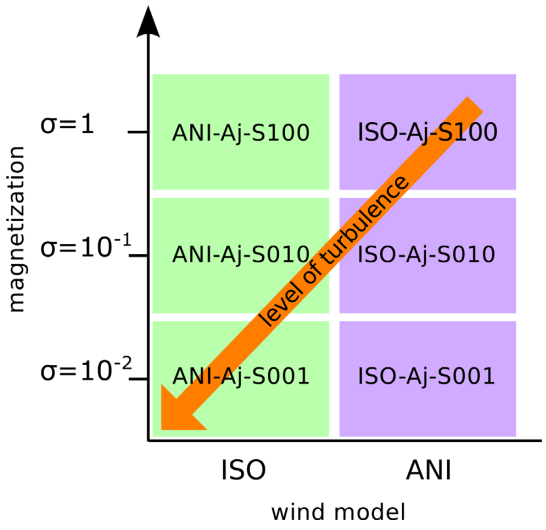

Figure 3. Notation used for the emission maps and its link with the value of magnetization and isotropy/anisotropy of the energy flux in the wind. ISO-A*j*-S*x* and ANI-A*j*-S*x* refer to the model $I_{\{\phi_M,\,i\}}$ and $A_{\{\phi_M,\,i\}}$ of Paper I, with $x = 10^{-i}$ referring to $\sigma = [0.01,\ 0.1,\ 1.0]$ and $j = 180(\phi_M/\pi)$ to the spin-to-kick inclination in degrees. This scheme also gives the indication of the development of turbulence in the different models (the orange arrow).

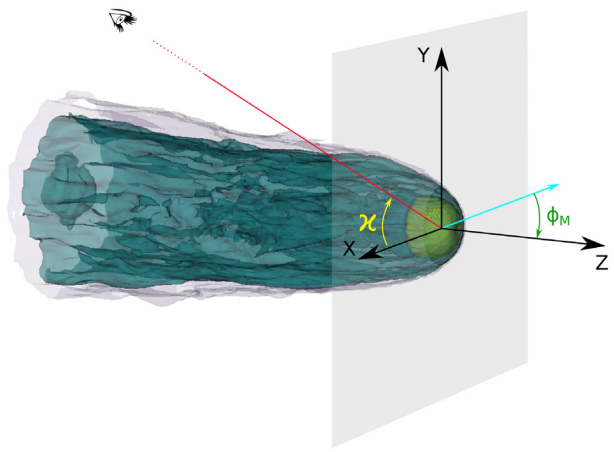

Figure 4. Representation of the angles considered in the discussion, with ϕ_M the inclination of the pulsar spin-axis with respect to its direction of motion (the z-axis) and $\mathcal{X}$ the inclination of the observer's line of sight in the x–y plane, superimposed on an isolevel model of a BSPWN made with the open source analysis tool VISIT (Childs et al. 2012).

only on the major trends, we limited our presentation here to few values of $\mathcal{X}$, typically $[0°, 45°, 90°]$, being the ones for which we do expect the largest differences. Moreover, we consider only a viewing geometry where the pulsar kick velocity lays on the plane of the sky.

3.1 Uniform wind luminosity

We begin our analysis with the fully axisymmetric case $I_{\{0,\,0\}}$, corresponding to an isotropic energy injection and a high magnetization value $\sigma = 1$. The dynamics in this case shows a low level of turbulence that only develops far away from the pulsar. For the sake of comparison with the laminar models, we first discuss the case of a uniform emissivity, deferring the case of an emissivity scaled by the pressure to the end, because the different choices in the normalization of the local emissivity mostly affect the emission maps, and not as much the polarization properties.

In this case the luminosity peaks in the head region, and is almost constant without any evidence for limb brightening (Fig. 5). The wings of the tail are about a factor of 2 brighter with respect to the core. The total emission has in this case a *jellyfish*-like morphology. These results are in reasonable agreement with the laminar models, except that there is no evidence for the slower region downstream of the Mach disc, which was found in the latter ones.

The PF is higher in the head, whose central part reaches values ∼0.9–0.8, with edges down to ∼0.2–0.3. There is some indication that the polarization rises again very close to the contact discontinuity (CD) up to values PF ∼ 0.7–0.9, but this might be due to spurious effect associated with the low surface brightness of those regions. In the tail the core has an average PF of 0.5 with local peaks up to 0.8, while the wings are depolarized (PF ∼ 0.2–0.3). This trend is in accordance with the findings of laminar models, even if the development of turbulence strongly reduces the PF. The polarized angle in the head is similar to the one of the laminar models, the tail has a core with the polarization orthogonal to the nebular axis, as expected for a toroidal field injected by a pulsar with spin-axis aligned with the kick velocity, while in the wings it tends to become aligned with the tail. This is due to a combination of local shear at the CD and relativistic polarization angle swing, which was already noted in the laminar case.

As the magnetization becomes smaller, Fig. 5 (bottom row), and turbulence increases, there is a change in the emission properties. For the case $I_{\{0,\,2\}}$, corresponding to a wind magnetization $\sigma = 0.01$, the luminosity is now more uniform with no apparent distinction between the core and the wings; the head tends to be underluminous; very fine structures appear in the luminosity maps on scales $\ll d_0$, probably related to the small-scale turbulence that is seen in the velocity maps (see Paper I). Here $d_0 = [\dot{E}/(4\pi c \rho_{ISM} v_{PSR}^2)]^{1/2}$ is the stand-off distance, the typical length scale of a BSPWN, depending on the pulsar luminosity ($\dot{E}$), kick velocity (v_{PSR}), and density of the ambient medium (ρ_{ISM}), with c the speed of light. The nebula is in general unpolarized, with perhaps some marginal residual polarization in the very head. The polarization maps again show the fine structures related to turbulence observed in the emission maps. There is a slightly higher polarized flux in the wings toward the CD. In general, no appreciable variation is seen with the inclination angle of the observer.

On the other hand if one assumes that the local emissivity scales with the local value of the gas pressure, the emission maps change substantially, while the results concerning the polarization properties do not as much, suggesting that it is just the structure of the magnetic field, more than the particle energy distribution, that regulates the polarization properties.

In Fig. 6, we show the total intensity for the cases $I_{\{0,\,0\}}$ and $I_{\{0,\,2\}}$, with the emissivity now weighted by the local pressure. The total emission, as well as the polarized emission, if far more enhanced in the head, where the pressure can be a factor of 10 or more higher than in the tail. In this case the luminosity is dominated by the very front part of the head, which can easily be a factor of 10–20 brighter than the tail, independently on the magnetization. The same holds in the low-σ case, where it is the very front of the bow shock that dominates the emission. The tail however is now slightly brighter in comparison to the high-σ case, partly reflecting the trend seen for a uniform emissivity, with no clear distinction between core and wings.

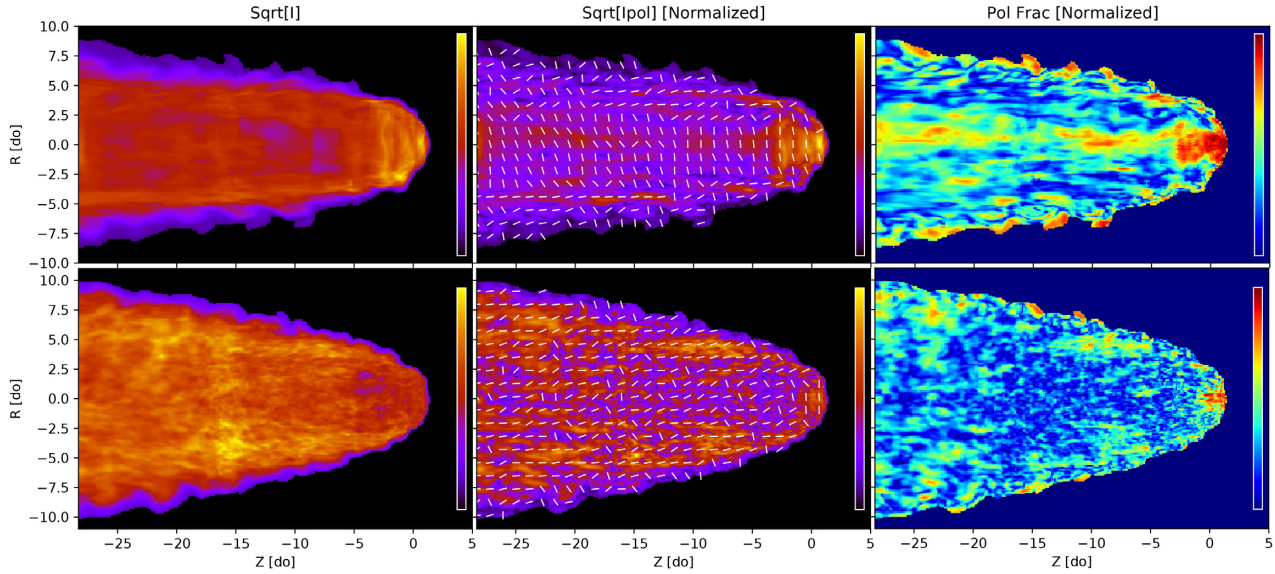

Figure 5. Maps for the case UNI-A00-S100 (upper row) and case UNI-A00-S001 (bottom row), with uniform local emissivity. From left to right: square root of the total synchrotron intensity normalized to the maximum, square root of the polarized intensity normalized to the maximum superimposed with the polarized direction, and polarized fraction (PF) normalized to the theoretical maximum for a power-law synchrotron with $\alpha = 0$. The colour scale is linear between zero and one.

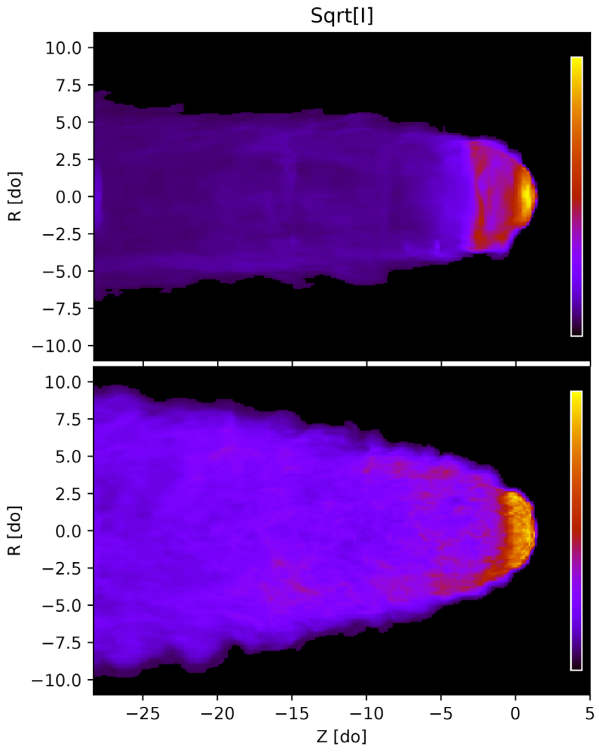

Figure 6. Maps computed assuming the local emissivity scales with the local value of the gas pressure. Square root of the total synchrotron intensity: upper panel for the UNI-A00-S100 case (to be compared with Fig. 5, upper panel); bottom panel for the UNI-A00-S001 case (to be compared with Fig. 5, bottom panel), both normalized to their maximum.

In the perpendicular case $\phi_{\rm M} = \pi/2$, instead we have analysed the emission properties for various values of the observer inclination angle $\mathcal{X}$. We begin again by discussing the case corresponding to a high magnetization $\sigma = 1$ and a uniform emissivity (case $I_{\{\pi/2,\,0\}}$), which has a more laminar structure and can be compared with those in Bucciantini (2018a). A set of maps computed for selected values of $\mathcal{X}$ is shown in Fig. 7.

We find that for all the possible values of $\mathcal{X}$, the tail brightness is higher in the wings than in the core by about a factor of 2. The difference is more pronounced at $\mathcal{X} = 90^\circ$. The head instead shows larger changes with the observer inclination. At $\mathcal{X} = 0^\circ$ it approximately has the same intensity of the tail, and looks quite uniform. As $\mathcal{X}$ increases to 90° it becomes brighter, with an enhanced limb right at the location of the CD, marking the position of the shocked pulsar wind in the head, between the termination shock and the CD itself. In terms of polarization properties the results are now reversed with respect to the aligned case: the PF is much higher in the wings and in the head with values up to 0.9, and reduced in the core of the tail that is almost depolarized for $\mathcal{X} = 90^\circ$. For $\mathcal{X} = 45^\circ$ the head looks slightly depolarized. The polarized angle instead looks fully aligned with the tail, with deviation of at most $\pm 15^\circ$, except in the $\mathcal{X} = 90^\circ$ case where in the head it looks orthogonal. These results are again consistent with those found using laminar models.

Lowering the magnetization, the flow becomes more turbulent and the overall appearance of the nebula, both in terms of total intensity and polarized properties, changes. For $\sigma = 0.01$, case $I_{\{\pi/2,\,2\}}$ (see Fig. 8), the nebula looks quite similar to the aligned case: the bulk of the head is less luminous than the tail, there are small-scales structure, and the level of polarization is small.

There is some residual evidence that the wings are slightly brighter than the core, and slightly more polarized (this is more evident for $\mathcal{X} = 90^\circ$). As expected for highly developed turbulence, the appearance and polarization properties do not depend much on the inclination angle with respect to the observer. At $\sigma = 0.1$, case $I_{\{\pi/2,\,1\}}$, we have an intermediate regime. The head has the same brightness as the core of the tail, while the wings are slightly brighter. In general for lower magnetizations we observe smaller scales in the polarization maps, and the PF has local patches as high as 0.8, with an average of about 0.6.

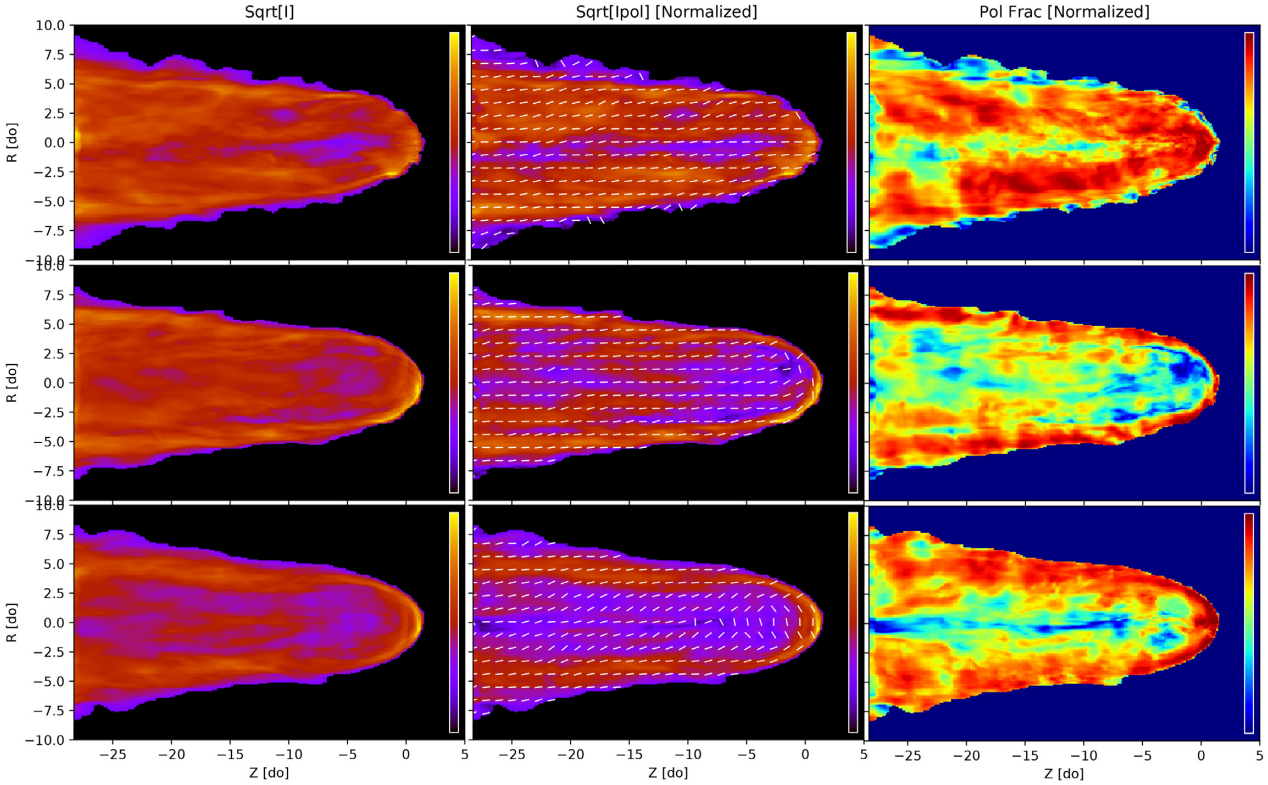

Figure 7. Same as Fig. 5, but here for the case UNI-A90-S100: top row for a viewing angle $\mathcal{X} = 0°$, middle row $\mathcal{X} = 45°$, and bottom row $\mathcal{X} = 90°$.

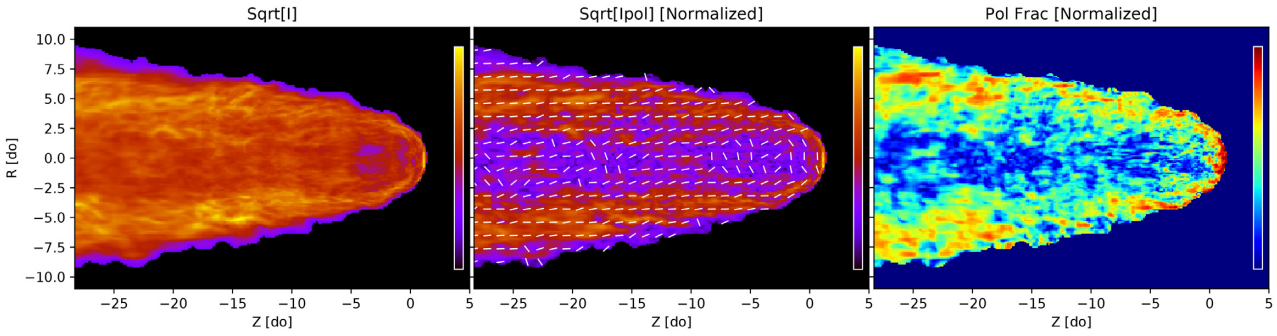

Figure 8. Same as Fig. 5, but here for the case UNI-A90-S001, with $\mathcal{X} = 90°$.

If instead one considers cases with the emissivity scaling with the pressure, one finds again that the polarized properties are essentially not much affected. What changes mostly is the emission pattern that now is dominated by a bright region in the very head, corresponding to the shocked layer between the termination shock and the CD, as shown in Fig. 9 for the case with the highest magnetization and $\mathcal{X} = 90°$.

This high brightness region is more pronounced in the high-σ regime than at lower magnetizations, where the head-to-tail brightness ratio tends to be smaller.

The case of a pulsar spin-axis inclined by $\phi_{\rm M} = 45°$ with respect to the kick velocity shows, in the high magnetization case $\sigma = 1$ ($I_{\{\pi/4,\,0\}}$) a variety of patterns in the emission and polarization properties that depends on the inclination angle of the observer (see Fig. 10).

For $\mathcal{X} = 0°$ (upper row of Fig. 10), the tail appears about a factor of 2 brighter than the head, and there is no wings-to-core difference. The polarization angle is aligned with the tail, and the PF is on

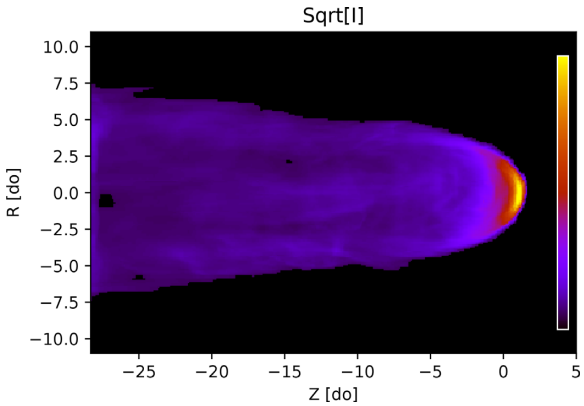

Figure 9. Map of the square root of the intensity computed assuming the local emissivity scales with the local value of the gas pressure, for the UNI-A90-S100 case, with a viewing angle $\mathcal{X} = 90°$.

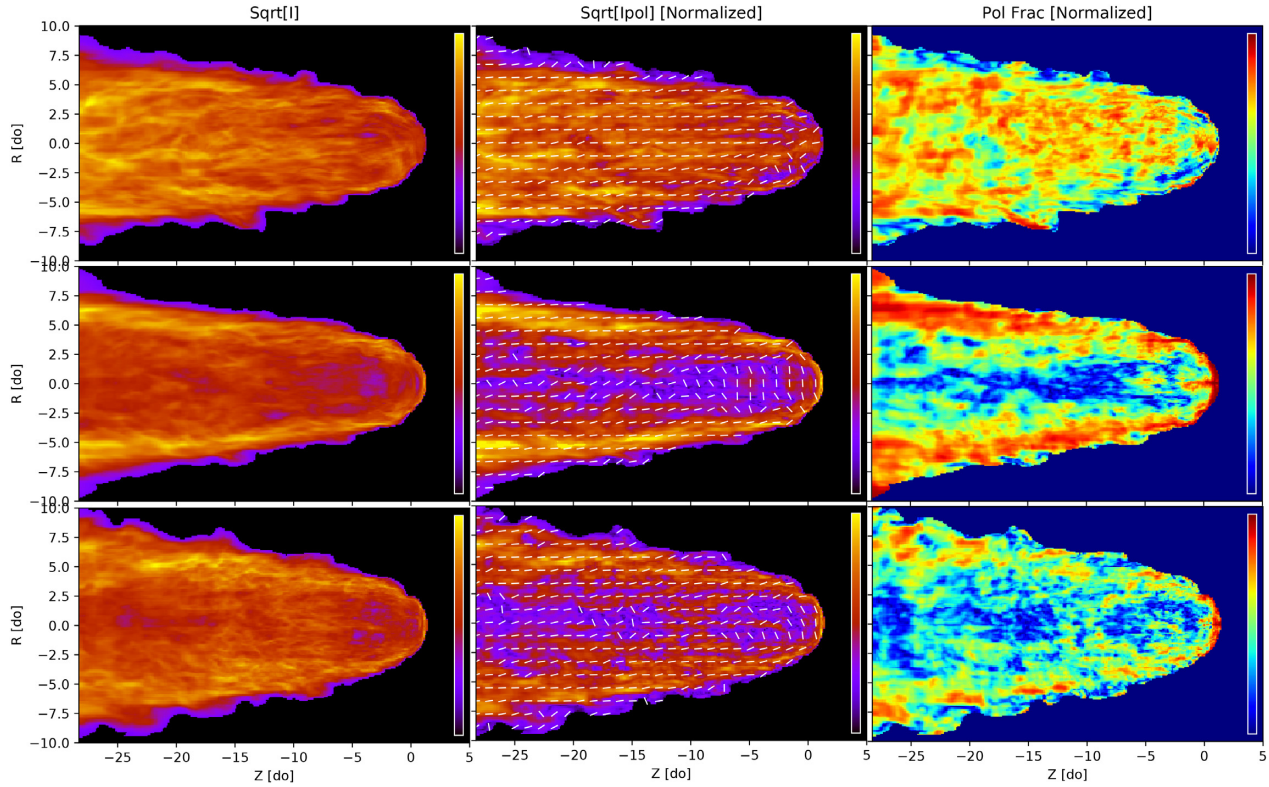

Figure 10. Same as Fig. 5, but in top row: case UNI-A45-S100 for a viewing angle $\mathcal{X} = 0°$; in middle row: case UNI-A45-S100 for $\mathcal{X} = 90°$; and in bottom row: case UNI-A45-S001 for $\mathcal{X} = 90°$.

average ∼0.6. As $\mathcal{X}$ increases towards 90°, as shown in the middle row of Fig. 10, the emission pattern increasingly resembles the orthogonal case, with brighter wings and a depolarized core. This is more markedly visible in the polarized intensity, which shows a very intense enhancement in the wings region and a limb brightening of the head. Given that the dynamics of this case is more turbulent than the previous ones, we observe the presence of lots of small structures in the maps of the PF. At low magnetization $\sigma = 0.01$ (bottom row of Fig. 10) the effect of turbulence is more pronounced, and the wind-to-core difference seen at $\mathcal{X} = 90°$ is far less evident. Polarization is in general smaller. Again, weighting the emissivity with the pressure leads to emission maps that are dominated by the very head, with a strong limb in the front of the system. Interestingly when $\mathcal{X} = 90°$ (see Fig. 11), the orthogonal case and the inclined one show very similar emission and polarization maps.

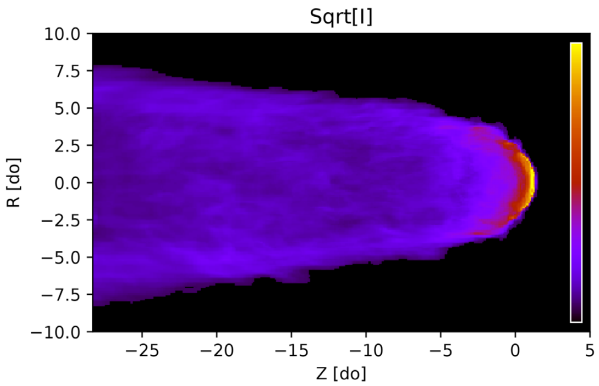

Figure 11. Map computed assuming the local emissivity scales with the local value of the gas pressure. Square root of the total synchrotron intensity for the UNI-A45-S100 case and $\mathcal{X} = 90°$.

3.2 Anisotropic wind luminosity

In Paper I, we investigated also cases with a pulsar wind energy flux dependent on the colatitude θ, according to a $F(\theta) \propto \sin^2\theta$ dependence, as expected for force-free split monopoles (Michel 1973; Bogovalov & Tsinganos 2001; Spitkovsky 2006). It was found that the flow in this case tends to show a higher level of turbulence, even at high magnetization ($\sigma = 1$).

We begin again discussing the high magnetization aligned case $A_{\{0,0\}}$, and the low magnetization one $A_{\{0,2\}}$, both shown in Fig. 12. Now at $\sigma = 1$ the intensity pattern looks quite different. The head is subluminous with respect to the tail, and the wings are brighter than the core. The intensity map shows the presence of long filamentary structures, while the overall polarization is small (PF $\sim$ 0.3) and there is no evidence for either a polarized head or a polarized core, as it was found for the isotropic wind luminosity. At low magnetization ($\sigma = 0.01$) instead the emission looks very similar to the isotropic case: the tail is brighter than the head; the wings are not markedly distinct from the core; and the nebula is almost completely depolarized. This same consideration apply also if one considers a local emissivity that scales as the local gas pressure. The only evident variation with respect to the isotropic injection case is that now the emission in the head is weaker, and the head-to-tail difference is less pronounced.

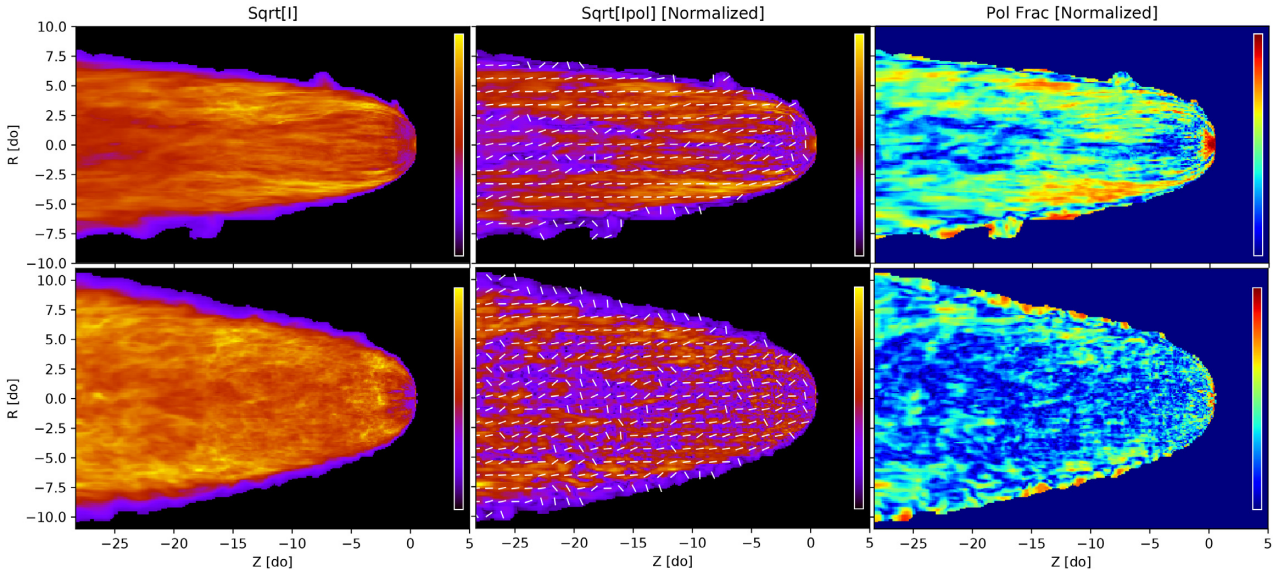

Figure 12. From left to right: square root of the total synchrotron intensity, square root of the polarized intensity, polarized fraction (PF); all normalized in terms of their maxima. The upper row refers to case ANI-A00-S100, while the bottom one to case ANI-A00-S001. The observer's viewing angle is in both cases $\mathcal{X} = 0^\circ$.

This same trends are also found for a spin-axis orthogonal to the kick velocity, $\phi_M = \pi/2$. The major differences with respect to the uniform injection case are that the head is basically fainter than the tail for all the possible inclinations of the observer, and for $\mathcal{X} = 0$ the wings-to-core brightness ratio tends to be stronger, as shown in Fig. 13.

The polarization pattern is quite similar to the uniform injection case, but the PF is in general a factor of 2–3 smaller, and characterized by the presence of fluctuations on small scales. These differences hold also in the $\sigma = 0.01$ case, where now the head is markedly fainter than the tail. For $\mathcal{X} = 0$ the wings are still brighter than the core, while for all the other observer inclination angles the tail luminosity looks quite uniform. The fact that for an anisotropic injection the head tends to be fainter implies that when one considers a case of local emissivity proportional to the local pressure, the observed enhancement of the head luminosity with respect to the tail one is less pronounced.

Far more interesting is the case of a spin-axis inclined by $\phi_M = 45^\circ$ with respect to the pulsar proper motion, cases $A_{\{\pi/4,\, i\}}$, shown for different magnetizations and viewing angles in Fig. 14. It was already noted in Paper I that this configuration was by far the most turbulent one, leading to major fluctuations in the shape of the bow shock, and triggering the formation of large blobs and waves propagating along the CD. All of this becomes particularly evident in the emission maps. The level of polarization is in general small, some residual global polarization ∼0.3 is still present at $\sigma = 1$, even if the polarization pattern can be very patchy, but at lower magnetization the nebula looks almost completely depolarized. At $\sigma = 1$ there is no difference in the intensity between the head and the tail, and overall the intensity maps do not show any distinction between wings and core. At $\sigma = 0.01$ the head is subluminous with respect to the tail even by a factor of a few. The global morphology of emission is also quite different when the direction of observation is varied.

If the local emissivity is weighed by the pressure, the head becomes again the dominant feature, but for $\sigma = 0.01$, patches in the tail with comparable luminosity can appear, as shown in Fig. 15.

3.3 Emission scaled with the currents

It has been suggested by several authors that current sheets and current layers could be important acceleration sites (Uzdensky, Cerutti & Begelman 2011; Cerutti et al. 2014; Lyutikov et al. 2016), and that they might play an important role in the origin of non-thermal particles in the turbulent environment of young PWNe. Here we investigate how the emission properties change if one assumes that the local synchrotron emissivity scales with the intensity of the local currents. In general the polarization properties (PF and angle) are not much affected, given that they depend of the overall magnetic structure of the system. We find that there is a tendency toward the formation of fine scales in the PF pattern, and that on average the PF of the various components (wings/core/head) tends to be slightly smaller, but these effects are only appreciable in high-resolution maps, while they disappear at lower resolutions. Major changes are seen mainly in the total emissivity: the head region tends in all cases to be brighter, and the emission morphology looks to be dominated by bright limbs close to the CD for the high magnetization $\sigma = 1$, and by a more uniform emissivity for the low magnetization $\sigma = 0.01$. Interestingly, apart for the aligned case, where this limb brightening is less evident, all the other cases show very similar emission morphology independent of the inclination angle of the pulsar spin-axis, or the orientation of the viewing angle. As anticipated, some effects of the AMR boxing are visible in the emission maps as changes in the average brightness, which drops as the resolution decreases. This is more likely due to the fact that our code does not include explicit resistivity, and the size, thickness, and intensity of the currents are solely regulated by numerical dissipation. Interestingly this effect is more pronounced in the very turbulent cases, and much less in the laminar ones, suggesting that as long as the flow remains laminar, the role of numerics in the dissipation of the magnetic field is weaker.

4 SUMMARY AND CONCLUSIONS

In this paper, we have studied the emission and polarimetric properties of BSPWNe based on the high-resolution numerical

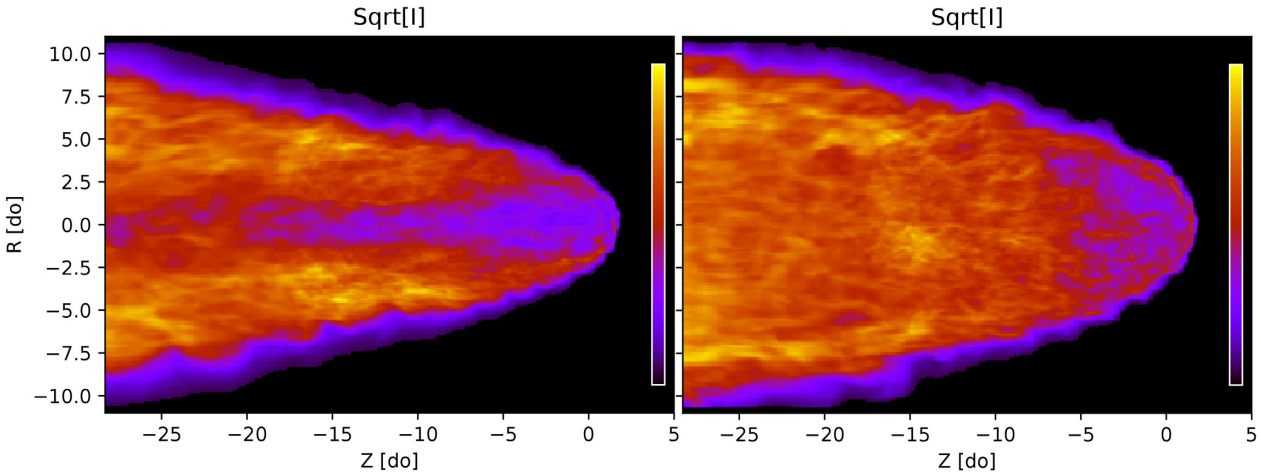

Figure 13. Square root of the total synchrotron intensity for case ANI-A90-S001, with $\mathcal{X} = 0^\circ$ (left-hand panel) and $\mathcal{X} = 90^\circ$ (right-hand panel).

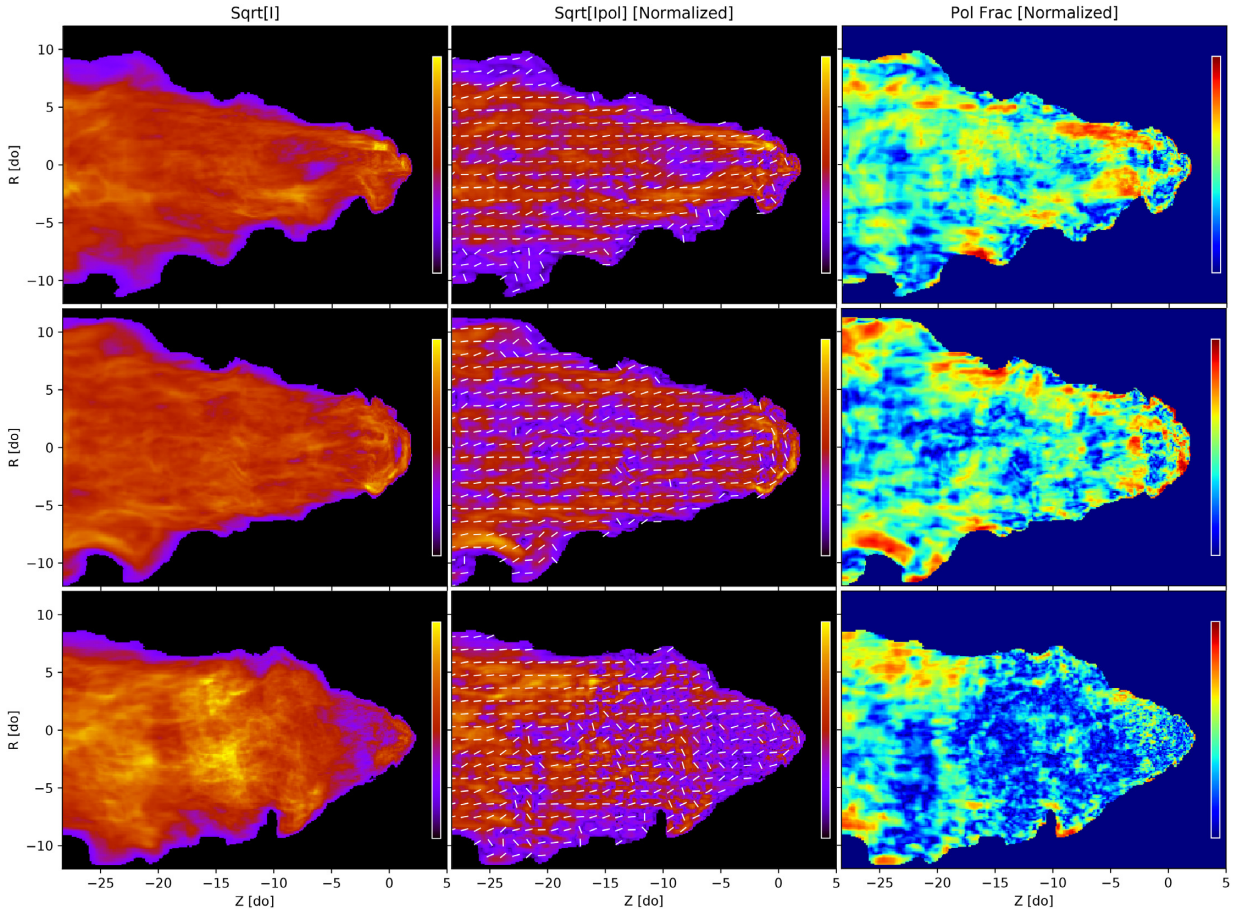

Figure 14. From left to right: square root of the total synchrotron intensity, square root of the polarized intensity, polarized fraction (PF); all normalized in terms of their maxima. The upper row refers to the case ANI-A45-S100 with $\mathcal{X} = 0^\circ$, the middle one to the case ANI-A45-S100 with $\mathcal{X} = 45^\circ$, and the bottom one to the case ANI-A45-S001 with $\mathcal{X} = 0^\circ$.

models presented and discussed in our previous work (Paper I), investigating and analysing a large set of different geometries of the BSPWNe.

While in that work the discussion was mostly focused on the flow pattern and the development of turbulence in the BSPWN tail, here we investigated those differences and their relation to the injection conditions in the pulsar wind, to see if they could be recovered from the properties of the emission, or if the emissivity is or not a good tracer of the wind properties.

We focused our discussion of the possible differences among various cases mostly to the case of high magnetization, where the flow is quasi-laminar and the structure in the tail preserves

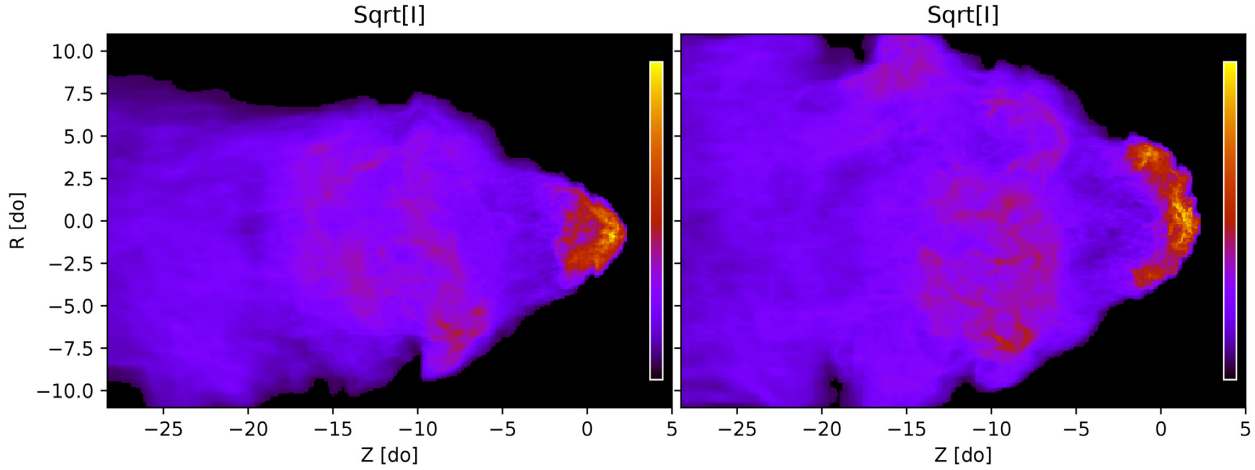

Figure 15. Square root of the total synchrotron intensity for cases ANI-A45-S001 $\mathcal{X} = 0°$ (left) and $\mathcal{X} = 90°$ (right).

information from the injection region in the head, while in low magnetized cases turbulence tends to wash out this information.

We found that in the case of uniform injection and high magnetization, there is indeed a strong correlation between the injection properties, as the inclination $\phi_{\rm M}$, and the surface brightness of our maps. The difference agrees with the expectation of fully laminar semi-analytic models of Bucciantini (2018a). We do observe a large variety of morphologies, from head dominated to tail dominated, with or without bright wings, and with different structures in the PF. The dependence on the viewing angle $\mathcal{X}$ is less marked and probably only appreciable at high resolution. In the high-σ regime the PF can be on average quite high in the tail. Once the magnetization drops we do see a drastic change towards a more turbulent regime. In this case it is far more difficult to find clear observational patterns that could be used to distinguish cases with different inclination $\phi_{\rm M}$ in a robust way.

An important characteristic of our maps is that, apart from the strongly turbulent cases $A_{\{\pi/4,i\}}$, we do not observe major fluctuation along the tail direction. This suggests that time variability associated with temporal changes in the flow pattern should not be strong, and we do not expect to see major changes in time in the emission from known objects. On the other hand, any detection of major changes in the shape or polarization properties of a BSPWN could be a clear indication for a strongly anisotropic energy injection and spin-axis misalignment.

Another important finding is related to the distribution of emitting particles. In all of our models, if we consider a scaling proportional to the local pressure, which is what one would naively expect for particles uniformly accelerated at the wind termination shock and then advected in the nebula, the head becomes much brighter that the tail, even by a factor of 10, and only in the most turbulent cases this difference is less enhanced. There are indeed systems like the Mouse nebula where a very bright head followed by a fainter tail is observed, but in many others there is no evidence for the head to be brighter than the tail (Yusef-Zadeh & Gaensler 2005; Ng et al. 2012). This could be the signature of a diffuse acceleration process, or of peculiar injection conditions at the termination shock. Interestingly there seems to be no appreciable difference between a uniform emissivity and an emissivity scaled according to the strength of the currents. This means that it will be hard to distinguish these two possibility just based on the emission pattern observed in known BSPWNe.

Another interesting aspect, related to polarization, is that in almost all cases the direction of the polarization (the inferred direction of the magnetic field) seems to be almost aligned with the tail (the only exception is for the orthogonal case with high magnetization). This is most likely due to polarization swing associated to the fast flow of matter in the tail. In fact if one turns down relativistic beaming and aberration, the structure of the polarization pattern changes, with a tendency to be less aligned. Changes in the polarization direction are observed in BSPWNe, often associated with changes in brightness (Ng et al. 2010). Our finding suggests that these could be due to rapid deceleration of the flow in the tail, arising either as a consequence of internal shocks, or because of mass loading from the CD. The level of polarization is instead a good indicator of turbulence, and generally scales with magnetization. This could explain why we see system with polarization as high as 60 per cent (Ng et al. 2012) and other as low as 10 per cent (Yusef-Zadeh & Gaensler 2005).

When magnetization is higher, and the dynamics in the tail is more laminar, the emission appears to be less uniform, peaking in the head region for the aligned case, $\phi_{\rm M} = 0$. When the inclination of the pulsar spin-axis $\phi_{\rm M}$ rises, the head starts to appear subluminous ($\phi_{\rm M} = 45°$), with some limb brightening close to the CD for higher inclinations, surrounding a still quite subluminous area ($\phi_{\rm M} = 90°$). The wings-to-core brightness also appears to increase with increasing $\phi_{\rm M}$.

The largest variety of morphologies in the maps are seen for the anisotropic wind cases, especially for the non-aligned models ($\phi_{\rm M} = 45°$, $\phi_{\rm M} = 90°$). Of particular interest is the anisotropic case with $\phi_{\rm M} = 45°$, which shows very different emission patterns when changing the observer's inclination angle, with an evident deformation from the canonical cometary shape of the other models, resembling somehow the observed conical shape of the Mouse nebula (at least in the inner part). The separation of the head and tail direction of the polarization vector also resembles what observed in the Mouse nebula when the observer's viewing angle is not zero (especially for $\mathcal{X} = 45°$), with a clear component wrapped around

the head and a general alignment with the nebular magnetic field in the tail.

We also computed a few maps considering a BSPWN where the pulsar velocity does not lie on the plane of the sky. Given the limit on the extent of the domain of our simulations, we can only compute configurations where the pulsar velocity is inclined at most 45° with respect to the plane of the sky (for higher inclinations we cannot integrate along the line of sight in the tail of the nebula without reaching the boundary of the numerical model). The inclination does not change the wings-to-core behaviour of our maps, while it rises the intensity of the tail with respect to the head. This can be easily understood in terms of integration along the line of sight. Given the cometary shape the inclination does not increase much the length of integration in the head, while it rises its value in the tail by an amount that is roughly inversely proportional to the cosine of the inclination angle. At $\mathcal{X} = 45°$ the tail is about twice brighter than in the orthogonal case shown in Section 3, while the head has approximately the same brightness.

ACKNOWLEDGEMENTS

We acknowledge the 'Accordo Quadro INAF-CINECA (2017–2019)' for the availability of high performance computing resources and support. Simulations have been performed as part of the class-A project 'Three-dimensional relativistic simulations of bow shock nebulae' (PI: B. Olmi). The authors acknowledge financial support from the 'Accordo Attuativo ASI-INAF n. 2017-14-H.0 Progetto: *on the escape of cosmic rays and their impact on the background plasma*' and from the INFN Teongrav collaboration. The authors wish to thank the referee, O. Toropina, for her timely and positive feedback on this work. B. Olmi acknowledges Andrea Mignone, from the PLUTO team, for fundamental support.

REFERENCES

Abeysekara A. U. et al., 2017, Science, 358, 911
Amato E., Blasi P., 2018, Adv. Space Res., 62, 2731
Arzoumanian Z., Chernoff D. F., Cordes J. M., 2002, ApJ, 568, 289
Arzoumanian Z., Cordes J., Van Buren D., Corcoran M., Safi-Harb S., Petre R., 2004, BAAS, 36, 951
Bandiera R., 1993, A&A, 276, 648
Barkov M. V., Lyutikov M., Khangulyan D., 2019, MNRAS, 484, 4760
Bell J. F., Bailes M., Manchester R. N., Weisberg J. M., Lyne A. G., 1995, ApJ, 440, L81
Blasi P., Amato E., 2011, Astrophys. Space Sci. Proc., 21, 624
Bogovalov S., Tsinganos K., 2001, Astron. Astrophys. Trans., 20, 303
Brownsberger S., Romani R. W., 2014, ApJ, 784, 154
Bucciantini N., 2002, A&A, 387, 1066
Bucciantini N., 2018a, MNRAS, 478, 2074
Bucciantini N., 2018b, MNRAS, 480, 5419
Bucciantini N., Bandiera R., 2001, A&A, 375, 1032
Bucciantini N., Olmi B., 2018, MNRAS, 475, 822
Bucciantini N., Amato E., Del Zanna L., 2005, A&A, 434, 189
Caraveo P. A., Bignami G. F., De Luca A., Mereghetti S., Pellizzoni A., Mignani R., Tur A., Becker W., 2003, Science, 301, 1345
Cerutti B., Werner G. R., Uzdensky D. A., Begelman M. C., 2014, Phys. Plasmas, 21, 056501
Chatterjee S., Gaensler B. M., Vigelius M., Cordes J. M., Arzoumanian Z., Stappers B., Ghavamian P., Melatos A., 2005, BAAS, 37, 1470
Chevalier R. A., Kirshner R. P., Raymond J. C., 1980, ApJ, 235, 186
Childs H. et al., 2012, in Bethel E. W., Childs H., Hansen C., eds, High Performance Visualization: Enabling Extreme-Scale Scientific Insight. Taylor & Francis, Abingdon, UK, p. 357
Cioffi D. F., McKee C. F., Bertschinger E., 1988, ApJ, 334, 252
Cordes J. M., Chernoff D. F., 1998, ApJ, 505, 315
Cordes J. M., Romani R. W., Lundgren S. C., 1993, Nature, 362, 133
De Luca A. et al., 2011, ApJ, 733, 104
Del Zanna L., Volpi D., Amato E., Bucciantini N., 2006, A&A, 453, 621
Dolch T., Chatterjee S., Clemens D. P., Cordes J. M., Cashmen L. R., Taylor B. W., 2016, J. Astron. Space Sci., 33, 167
Gaensler B. M., 2005, Adv. Space Res., 35, 1116
Gaensler B. M., Slane P. O., 2006, ARA&A, 44, 17
Gaensler B. M., van der Swaluw E., Camilo F., Kaspi V. M., Baganoff F. K., Yusef-Zadeh F., Manchester R. N., 2004, ApJ, 616, 383
Ghavamian P., Raymond J., Smith R. C., Hartigan P., 2001, ApJ, 547, 995
Hales C. A., Gaensler B. M., Chatterjee S., van der Swaluw E., Camilo F., 2009, ApJ, 706, 1316
Hester J. J., Raymond J. C., Blair W. P., 1994, ApJ, 420, 721
Hui C. Y., Becker W., 2007, A&A, 467, 1209
Jakobsen S. J., Tomsick J. A., Watson D., Gotthelf E. V., Kaspi V. M., 2014, ApJ, 787, 129
Johnson S. P., Wang Q. D., 2010, MNRAS, 408, 1216
Jones D. H., Stappers B. W., Gaensler B. M., 2002, A&A, 389, L1
Kargaltsev O., Misanovic Z., Pavlov G. G., Wong J. A., Garmire G. P., 2008, ApJ, 684, 542
Kargaltsev O., Pavlov G. G., Durant M., 2012, in Lewandowski W., Maron O., Kijak J., eds, ASP Conf. Ser. Vol. 466, Electromagnetic Radiation from Pulsars and Magnetars. Astron. Soc. Pac., San Francisco, p. 167
Kargaltsev O., Pavlov G. G., Klingler N., Rangelov B., 2017, J. Plasma Phys., 83, 635830501
Klingler N., Kargaltsev O., Rangelov B., Pavlov G. G., Posselt B., Ng C.-Y., 2016a, ApJ, 828, 70
Klingler N. et al., 2016b, ApJ, 833, 253
Klingler N., Kargaltsev O., Pavlov G. G., Ng C.-Y., Beniamini P., Volkov I., 2018, ApJ, 861, 5
Kulkarni S. R., Hester J. J., 1988, Nature, 335, 801
Leahy D., Green K., Tian W., 2014, MNRAS, 438, 1813
Li X. H., Lu F. J., Li T. P., 2005, ApJ, 628, 931
Lyutikov M., Sironi L., Komissarov S., Porth O., 2016, preprint (arXiv: 1603.05731)
Marelli M. et al., 2013, ApJ, 765, 36
Marelli M., Tiengo A., De Luca A., Mignani R. P., Salvetti D., Saz Parkinson P. M., Lisini G., 2019, A&A, 624, A53
Michel F. C., 1973, ApJ, 180, L133
Misanovic Z., Pavlov G. G., Garmire G. P., 2008, ApJ, 685, 1129
Morlino G., Lyutikov M., Vorster M., 2015, MNRAS, 454, 3886
Ng C. Y. et al., 2009, BAAS, 41, 307
Ng C.-Y., Gaensler B. M., Chatterjee S., Johnston S., 2010, ApJ, 712, 596
Ng C.-Y., Bucciantini N., Gaensler B. M., Camilo F., Chatterjee S., Bouchard A., 2012, ApJ, 746, 105
Olmi B., Bucciantini N., 2019, MNRAS, 484, 5755 (Paper I)
Olmi B., Del Zanna L., Amato E., Bandiera R., Bucciantini N., 2014, MNRAS, 438, 1518
Olmi B., Bucciantini N., Morlino G., 2018, MNRAS, 481, 3394
Pavan L. et al., 2014, A&A, 562, A122
Pavlov G. G., Sanwal D., Zavlin V. E., 2006, ApJ, 643, 1146
Pavlov G. G., Bhattacharyya S., Zavlin V. E., 2010, ApJ, 715, 66
Posselt B. et al., 2017, ApJ, 835, 66
Rangelov B., Pavlov G. G., Kargaltsev O., Durant M., Bykov A. M., Krassilchtchikov A., 2016, ApJ, 831, 129
Romani R. W., Slane P., Green A. W., 2017, ApJ, 851, 61
Sánchez-Cruces M., Rosado M., Fuentes-Carrera I., Ambrocio-Cruz P., 2018, MNRAS, 473, 1705
Sartore N., Ripamonti E., Treves A., Turolla R., 2010, A&A, 510, A23
Spitkovsky A., 2006, ApJ, 648, L51
Truelove J. K., McKee C. F., 1999, ApJS, 120, 299
Uzdensky D. A., Cerutti B., Begelman M. C., 2011, ApJ, 737, L40
van der Swaluw E., Achterberg A., Gallant Y. A., Downes T. P., Keppens R., 2003, A&A, 397, 913

van Kerkwijk M. H., Kulkarni S. R., 2001, A&A, 380, 221
Verbunt F., Igoshev A., Cator E., 2017, A&A, 608, A57
Vigelius M., Melatos A., Chatterjee S., Gaensler B. M., Ghavamian P., 2007, MNRAS, 374, 793
Volpi D., Del Zanna L., Amato E., Bucciantini N., 2008, A&A, 485, 337
Wang Z., Kaplan D. L., Slane P., Morrell N., Kaspi V. M., 2013, ApJ, 769, 122
Wilkin F. P., 1996, ApJ, 459, L31
Wong D. S., Cordes J. M., Chatterjee S., Zweibel E. G., Finley J. P., Romani R. W., Ulmer M. P., 2003, in Li X. D., Trimble V., Wang Z. R., eds, Proc. IAU Symp. 214, High Energy Processes and Phenomena in Astrophysics. Astron. Soc. Pac., San Francisco, p. 135
Yusef-Zadeh F., Bally J., 1987, Nature, 330, 455
Yusef-Zadeh F., Gaensler B. M., 2005, Adv. Space Res., 35, 1129

This paper has been typeset from a TEX/LATEX file prepared by the author.